High-Intensity Focused Ultrasound (HIFU) Modeling:In Vitro Validation and Integration into Patient-Specific Planning Tool

Fabio Morelli
Politecnico di Milano
Alessandro Albanesi
alessandro.albanesi@polimi.it

Politecnico di Milano
Alice Ivanaj
Politecnico di Milano
Silvia Buratti
Sant'Anna School of Advanced Studies
Francesca Parrotta
Sant'Anna School of Advanced Studies
Junling Fu
Politecnico di Milano
Selene Tognarelli
Sant'Anna School of Advanced Studies
Arianna Menciassi
Sant'Anna School of Advanced Studies
Elena De Momi
Politecnico di Milano
Alberto Redaelli
Politecnico di Milano

Article

Keywords:

Posted Date: September 5th, 2025

DOI: https://doi.org/10.21203/rs.3.rs-7427702/v1

Additional Declarations: No competing interests reported.

High-Intensity Focused Ultrasound (HIFU) Modeling: In Vitro Validation and Integration into Patient-Specific Planning Tool

Fabio Morelli[1,+], Alessandro Albanesi[1,+,*], Alice Ivanaj[1], Silvia Buratti[2], Francesca Parrotta[2], Junling Fu[1], Selene Tognarelli[2], Arianna Menciassi[2], Elena De Momi[1], and Alberto Redaelli[1]

[1]Department of Electronics, Information and Bioengineering, Politecnico di Milano, Italy
[2]The BioRobotics Institute, Scuola Superiore Sant'Anna, 56127 Pisa, Italy.
[*]alessandro.albanesi@polimi.it
[+]these authors contributed equally to this work

ABSTRACT

This study aims at developing and experimentally validate a three-dimensional numerical model designed to predict acoustic propagation and thermal effects during High-Intensity Focused Ultrasound (HIFU) therapy, in order to support patient-specific treatment planning. A 3D time-domain simulation was implemented using the k-Wave toolbox, capturing both acoustic wave propagation and thermal effects. Validation was performed using five tissue-mimicking phantoms with distinct acoustic and thermal properties, each tested under three different HIFU exposure conditions. Lesion dimensions were assessed longitudinally and transversely in both simulations and experiments, and spatial concordance was quantified by evaluating the overlap between simulated and experimental lesions. Simulated longitudinal lesion extents fell within the interquartile range of experimental data in five out of nine phantom-condition combinations with a maximum absolute error of 2.70 mm while transverse dimensions in three out of nine with maximum absolute error equal to 4.16 mm. Spatial overlap between simulated and experimental lesions reached a maximum of 92%. Simulations on phantoms required approximately 16 minutes, while patient-specific cases completed in about 32 minutes, accurately capturing heterogeneous tissue characteristics and bone interfaces. In scenarios involving rib intersection, a 40% reduction in focal pressure was observed, leading to significant smaller lesions. The validated 3D simulation, integrated into a planning platform, reliably predicts HIFU ablation zones and focal shifts, showing strong agreement with experimental data and delivering results within clinically feasible times.

Introduction

High-Intensity Focused Ultrasound (HIFU) is a non-invasive, extracorporeal therapeutic modality to non invasively treat many medical disorders, such as tumors and neurological diseases[1,2]. It operates by using piezoelectric transducers to concentrate ultrasound (US) waves to a precise target within the patient's body. At the focal point, the convergent beams create a highly localized energy deposition that induces thermal ablation and/or mechanical effect[3], without damaging the surrounding healthy tissues[4–6]. HIFU offers several advantages over conventional surgery: reduced procedural pain, lower costs, faster recovery times, absence of residual scarring, no dose limitations, and avoidance of ionizing radiation[7]. Effective HIFU-based treatments rely on integrating imaging modalities for guidance and real-time monitoring. Two primary approaches are Magnetic Resonance (MRgHIFU) and Ultrasound guidance (USgHIFU)[8]. MRI guidance provides excellent soft tissue contrast and allows temperature monitoring during HIFU procedures. However, combining HIFU therapy with MRI scanners requires complex and expensive equipment. In contrast, USgHIFU offers several advantages such as ease of use, lower costs, portability, broader patient access, and the capability for rapid imaging, thereby enabling real-time treatment adjustments and usability in intraoperative scenario. Early USgHIFU platforms were bulky and manually operated, which limited transducer mobility, reduced accessibility to treatment sites, and compromised targeting precision. Recent solutions explore the use of actively controlled robotic arms to overcome these issues achieving greater flexibility, enhanced targeting accuracy, and increased treatment reproducibility[6,8,9]. Although HIFU has demonstrated efficacy in non-invasive tumor ablation, several limitations arise from both anatomical and physiological complexities of tissues:

1. Discrepancy Between Geometrical and Actual Focus: Tissue heterogeneity shifts the actual focal point away from the transducer's geometric focus, reducing treatment accuracy[10–13].

2. Ribcage and Bone Interference: Bones absorb and reflect ultrasound, lowering energy transmission and heightening the risk of off-target heating[14].

3. Perfusion Effects: High blood flow in major vessels disperses heat, diminishing treatment efficacy and potentially harming blood vessels[15].

4. Organ Motion: Respiratory and cardiac activity complicates target alignment, often necessitating motion compensation or repeated treatments[16,17].

5. Limited Penetration and Focal Depth: Deep or large tumors may not receive sufficient energy, due to dispersion, requiring prolonged sonication times or multiple sessions.

6. Learning Curve: Accurate dose adjustment relies heavily on operator expertise, thereby increasing the complexity of the HIFU procedure and making precise modulation of the therapeutic dose more challenging.

To mitigate these limitations, different strategies have been proposed, including hardware enhancements with beam-steering transducers[18,19], acoustic lens for aberrations correction[20], robot control for motion compensation[9,16], and simulation-based planning for accurate lesion prediction.

Several strategies have been proposed in the literature to simulate HIFU treatments, with the goal of improving treatment planning and clinical outcomes. Daniel et al.[21] and Safisamghabadi et al.[22] have shown the feasibility of modeling both acoustic and thermal fields exploiting the Finite Element Method (FEM) in COMSOL Multiphysics (COMSOL Inc.[23]). However, these works are limited to two-dimensional (2D) models, which fail to fully capture anatomical asymmetries and complex tissue heterogeneities.

Moreover, experimental validation is frequently lacking, and when performed, it often reveals poor reproducibility of the HIFU technology in terms of focal point localization and lesion size[5]. An emerging alternative is the open-source *k-Wave* toolbox[24], which allows for 3D simulations, solving the Westervelt equation using the k-space pseudo-spectral method. Martin *et al.*[25] reported a peak pressure estimation error of approximately 10% when comparing *k-Wave* simulations to experimental data in inhomogeneous media. Although these results support the predictive capabilities of the tool, validation was limited to pressure measurements in a single material, without assessing thermal lesion formation. The same toolbox was exploited also by Rosnitskiy *et al.*[26], who developed a graphical user interface (GUI) software to visualize a CT-based patient-specific 3D acoustic model of the subject's anatomy and determine the optimal positioning of the HIFU source, though without experimental validation. In both cases, simulations are computationally intensive, often requiring hours on multi-GPU clusters, preventing their applicability in intraoperative settings[25].
The presented work aims at addressing these limitations by developing and *in vitro* validating a fast 3D numerical model for predicting acoustic propagation and thermal effects during HIFU therapy. The study has four main objectives: (i) accurately localize the HIFU focal point, (ii) estimate the spatial extent of the resulting thermal lesions, (iii) carry out an *in vitro* validation and (iv) develop a Graphical User Interface (GUI) to visualize the simulated focal point within a 3D environment that includes both the transducer and the patient-specific anatomy reconstructed from CT data, supporting intuitive and informed treatment planning.

Methods

This section outlines the methodologies and materials employed in this study, including the computational models for acoustic and thermal simulations, the experimental setup for model validation, and the development of a GUI for visualization and treatment planning from patient specific anatomies.

Computational Framework for Acoustic and Thermal Simulation

We used k-Wave (MATLAB toolbox) to implement a 3D time-domain simulation of propagating acoustic waves and thermal effects[27]. The toolbox solves a set of coupled first-order partial differential equations based on conservation laws and the material's frequency-dependent acoustic absorption behavior, governed by a frequency power law:

$$\alpha = \alpha_0 f^y \tag{1}$$

where α is the absorption coefficient (dB/cm), α_0 is the power law prefactor (dB/(MHz·cm)), f is the ultrasound frequency (MHz), and y is the power law exponent. The fundamental equations can be summarized as:

$$\frac{\partial \mathbf{u}}{\partial t} = -\frac{1}{\rho_0}\nabla p, \tag{2}$$

$$\frac{\partial \rho}{\partial t} = -(2\rho + \rho_0)\,\nabla\cdot\mathbf{u} - \mathbf{u}\cdot\nabla\rho_0, \tag{3}$$

$$p = c_0^2\Big(\rho + \mathbf{d}\cdot\nabla\rho_0 + \frac{B}{2A}\frac{\rho^2}{\rho_0} - L\rho\Big) \tag{4}$$

where p is the acoustic pressure (Pa), u is the particle velocity (m/s), ρ (Kg/m^3) represents the deviation of the medium's density from its equilibrium value ρ_0 due to waves propagation, and d is the particle displacement (m). Nonlinear effects, significant in HIFU therapy, are accounted for by the nonlinearity parameter (B/A), which quantifies how sound speed varies with pressure. L captures dispersion and frequency-dependent absorption, expressed as:

$$L = -2\alpha_0\, c_0^{(y-1)}\,\frac{\partial}{\partial t}\left(-\nabla^2\right)^{\left(\frac{y}{2}-1\right)} + 2\alpha_0\, c_0^{y}\tan\!\left(\tfrac{\pi y}{2}\right)\left(-\nabla^2\right)^{\left(\frac{y+1}{2}-1\right)} \tag{5}$$

These equations generalize the Westervelt equation[28] to account for medium heterogeneity and are solved using a k-space pseudo-spectral method. Additionally, we incorporated a particle velocity field, allowing for the computation of acoustic intensity, which is crucial for estimating the heating effect of ultrasound in biological tissues.

Once the pressure field is computed, the heat source power density (Q) is derived as:

$$Q = \frac{\alpha(2\pi)^2 p^2}{2\rho c} \tag{6}$$

which serves as an input for the Pennes' Bioheat Equation, modeling heat transfer:

$$\rho C\frac{\partial T}{\partial t} = k\nabla^2 T + Q \tag{7}$$

where C is specific heat capacity (J/(kg·K)), k is thermal conductivity (W/(m·K)), and T is temperature (K).

In this work, we considered as ablated region in the medium the one exceeding the temperature of 60°[2,6] . We implemented a fully 3D simulation that enabled us to characterize the ablated lesion using three principal dimensions, thereby avoiding any simplification based on symmetry. The major axial dimension (D1) represents the lesion height along the HIFU beam propagation direction, whereas the major transverse dimensions (D2 and D3) correspond to the maximum axis of the lesion's section in the plane perpendicular to the beam.

K-Wave simulation environment requires four key input: i) Medium Properties, ii) Transducer Configuration, iii) Computational Grid, iv) Sensor Configuration.

Medium Properties

i.e. geometry, density, sound speed, attenuation power law, nonlinearity (B/A), specific heat capacity, and thermal conductivity.

Transducer Definition

We modeled a single-element transducer with a diameter of 12 cm, a radius of curvature of 12 cm, and a central hole of 3.5 cm. The emitted signal was defined as a continuous sinusoidal wave (CW), mathematically expressed as:

$$s(t) = amp(i,j)\cdot\sin\left(2\pi f t + \phi(i,j)\right) \tag{8}$$

where amp, f and ϕ are the signal amplitude, frequency and phase respectively. We set the transducer operating frequency and the maximum amplitude at 1.2 MHz and 0.33 MPa respectively. The transducer power in the simulation was set based on Equation 9:

$$P = \frac{amp^2\cdot A}{2\rho\upsilon} \tag{9}$$

where P (W) is the power of the transducer, amp (Pa) is the amplitude of the transducer's signal and A (m^2) is the projected area of the transducer.

Computational Grid - Spatial and Temporal Resolution

Upon conducting a mesh sensitivity analysis, we selected the optimal spatial resolution as the one that achieved a balance between computational efficiency and solution convergence. The grid spacing was set to $0.3 \times 0.3 \times 0.3$ *mm*, which satisfied the resolution criterion of $\lambda_w/3$, a condition proven to be sufficient for accurate k-Wave simulations[26]. Here, λ_w represents the acoustic wavelength, defined as v_w/f, where $f = 1.2$ MHz is the transducer frequency, and v_w is the average sound speed in the mediums. We set the time step dt as:

$$dt = \frac{CFL \cdot dx}{v_M} \tag{10}$$

where dx is the spatial grid step, and v_M is the maximum sound speed in the mediums and CFL is the Courant–Friedrichs–Lewy stability condition, with a *CFL number* of 0.3, ensuring numerical stability[27].
To enhance the computational efficiency and reduce processing time, achieving near real-time performance, we implemented the following optimization strategies:

1. Single Precision Computation: We conducted the simulations in single precision instead of default double precision, improving computational speed by approximately 1.5 to 1.6 times[27].
2. GPU Acceleration: We executed the simulations on an NVIDIA GeForce RTX 4090 GPU with 24 GB of RAM. MATLAB's Parallel Computing Toolbox enabled GPU-based processing.
3. Simulation Time: We set the simulated time to ensure the achievement of the steady-state condition of the ultrasound beam:

$$\Delta T_{\text{simulated}} = \frac{s_d}{v_m} \tag{11}$$

s_d represents the longest ultrasound beam trajectory within the computational domain (14x13x13 cm), and v_m is the minimum sound speed in the domain. The computational domain size was chosen to include the transducer and its geometrical focus, with a limited margin to prevent an excessive increase in computational cost.

Experimental Protocol

We conducted an *in vitro* validation of the HIFU treatment simulation using five distinct tissue-mimicking phantoms, in an experimental setup comprising a robotic HIFU platform (Figure 2).

Phantom crafting

The phantoms used in the experiments are shown in Figure 1. They consist of a common bottom layer of Polyacrilammide (PA) hydrogel + albumin[29] (3 cm) and different top layers[30–33] (0.5 cm). The crafting protocol and the acoustic and thermal properties of the materials are reported in Table 1. We designed the phantoms based on the following criteria:

- Echogenic and homogeneous materials;
- Thermal and acoustic characterization of materials in the state of the art;
- Simple and well-defined geometry to ensure consistency with the virtual models used in the simulation;
- Smooth surfaces to avoid unwanted beam refractions or aberrations due to irregularities.

The PA material was chosen for its transparency and thermosensitive properties. Due to the presence of albumin, the material undergoes denaturation when exposed to temperatures exceeding 60°C, thus changing color and ensuring clear visualization of the ablated area. The same geometry and material acoustic and thermal properties were used to define the corresponding virtual models in the numerical simulation.

Experimental setup

The sonication experiments were performed by using the robotic platform for USgHIFU surgery in Figure 2. To achieve high-precision positioning of the HIFU transducer, the device was rigidly affixed to the end-effector of a six-degree-of-freedom (6-DoF) robotic manipulator (M0609, Doosan, Korea). The HIFU transducer, a 16-channel phased annular array (Imasonic, Voray-sur-l'Ognon, France), featured a diameter of 120 mm, a radius of curvature of 120 mm, and a central aperture of 35 mm. It was driven by a 16-channel high power signal generator (Image Guided Therapy, Pessac, FR) with each channel independently capable of delivering up to 20 W of acoustic power, corresponding to a maximum amplitude of 0.33 MPa,

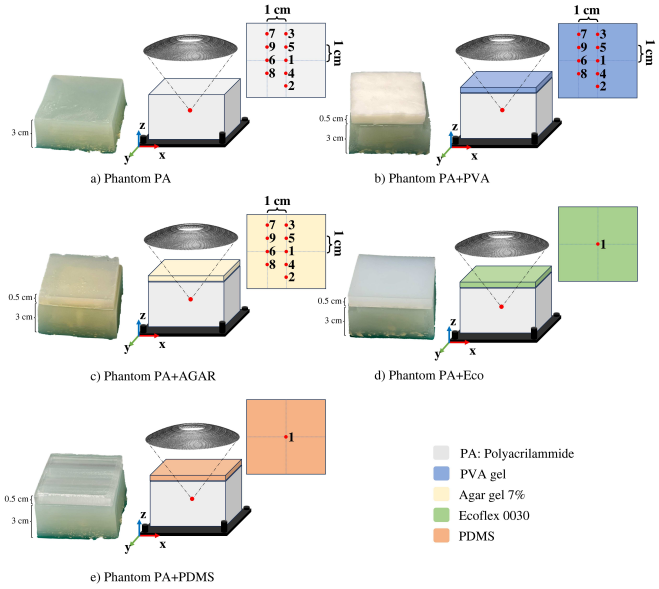

Figure 1. Custom tissue-mimicking phantoms used for experimental validation with their corresponding simulated counterpart. For each phantom, the material composition, the layers dimension and corresponding sonication pattern are reported. The transducer illustration does not reflect its actual dimensions and has been scaled for visualization purposes.

Property	Water	PA Gel	Agar Gel	PVA	Ecoflex	PDMS
Density (kg/m^3)	1000	1044	1060	1090	1070	1042
Sound Speed (m/s)	1500	1544	1510	1543	967	1055
Attenuation (dB/cm @ 1.2 MHz)	0.002	0.17	0.25	0.085	2.54	3.08
Nonlinearity (B/A)	5.2	4.9	–	–	–	–
Specific Heat (J/kg·K)	4180	5100	4200	3211	1615	1615
Thermal Conductivity (W/m·K)	0.6	0.7	0.53	0.36	0.20	0.20
Crafting						
Protocol	–	29	30	31	32	33
Crafting Time (hours)	–	3	0.5	72	6	48
Conservation Time (weeks)	–	3	4	52	Stable	Stable

Table 1. Acoustic and thermal properties of the materials used in the HIFU experiments.

yielding a cumulative maximum output of 320 W. A 2D linear phased-array ultrasound probe, operating within a 4–7 MHz bandwidth, was coaxially integrated within the central aperture of the HIFU transducer to enable real-time monitoring during sonication. The geometric focus of the HIFU beam could be electronically adjusted via axial steering within a range of ±20 mm, enabling a variable focal depth between 100 mm and 140 mm along the axial axis. The entire assembly, including the transducer, imaging probe, and tissue-mimicking phantoms, was immersed in a water tank filled with degassed and deionized water (dd-H_2O) to ensure optimal acoustic transmission and to mitigate wavefront distortion and energy loss. A dedicated mounting platform was engineered to ensure the stable and reproducible placement of the phantoms at the base of the tank. The platform comprised a foundational layer of acoustic-absorptive material, employed to suppress acoustic reflections and to prevent the emergence of secondary focal zones. A 3D-printed frame, positioned above the absorber, served as a housing for the phantoms and geometric reference for robotic calibration procedures. The phantoms were subsequently affixed to this platform using a pair of magnetically anchored, detachable arms specifically designed to preserve the integrity of the acoustic field by minimizing interference with wave propagation.

The initial positioning of the HIFU transducer was established by aligning its geometric focus with the center of the phantom. To ensure accurate spatial alignment, a calibration procedure was conducted to determine the rigid transformation between the robot base coordinate system F_{base} and the phantom coordinate system F_{phantom}, defined at the corner of the 3D-printed calibration frame. This procedure yielded the homogeneous transformation matrix ${}^{\text{base}}T_{\text{phantom}}$.

The calibration frame featured four pillars of varying heights with grooves on top. The physical coordinates of these grooves,

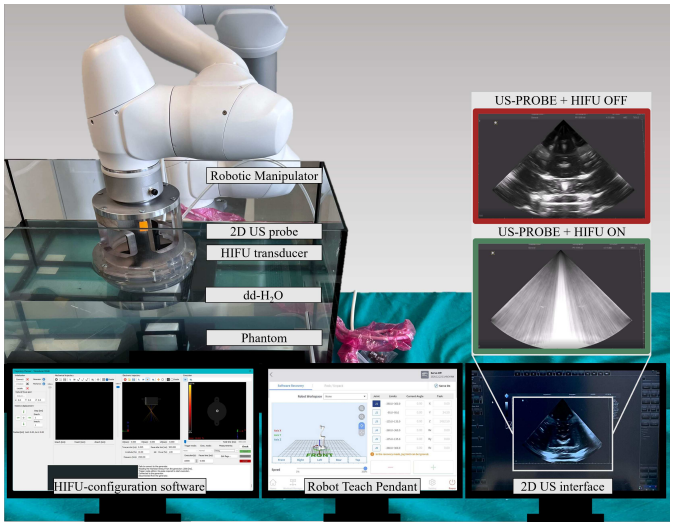

Figure 2. Experimental setup including the robotic manipulator holding the HIFU transducer, a water tank filled with dd-H_2O, and the phantom secured to the bottom-mounted support. On the right, a laptop displaying real-time US monitoring images acquired by the 2D US probe. On the center, the interface controlling the robot positioning. On the left, the laptop running the software for setting the HIFU sonication parameters.

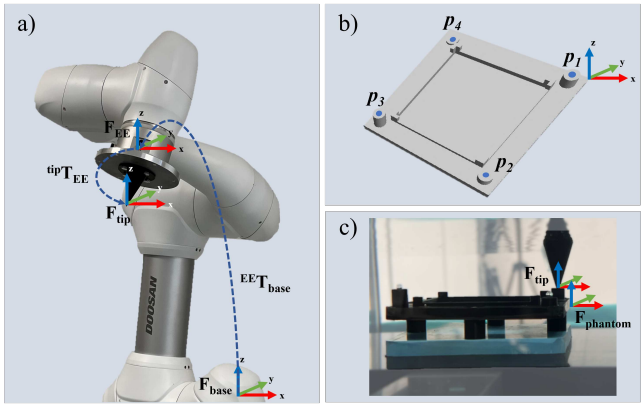

Figure 3. Calibration setup showing the 3D-printed frame with four grooved pillars, used to compute the transformation between the robot base and the simulation environment.

denoted as ${}^{\text{phantom}}\mathbf{p}_i, \quad i = 1,2,3,4$ were measured in the F_{phantom} (Figure 3.b). The same physical points were acquired by placing the tip of a pointer, rigidly attached to the robot's end-effector, in the corresponding grooves (Figure 3.c). The pointer tip coordinates ${}^{\text{tip}}\mathbf{p}_i$ were expressed with respect to the robot base by combining the forward kinematics ${}^{\text{base}}T_{\text{ee}}$ and the known geometry of the pointer ${}^{\text{ee}}T_{\text{tip}}$ (Figure 3.a):

$$ {}^{\text{base}}T_{\text{tip}} = {}^{\text{base}}T_{\text{ee}} \cdot {}^{\text{ee}}T_{\text{tip}} \tag{12} $$

Applying the transformation in Eq.(12), the positions of the four detected grooves in the robot base frame were computed as:

$$ {}^{\text{base}}\mathbf{p}_i = {}^{\text{base}}T_{\text{tip}} \cdot {}^{\text{tip}}\mathbf{p}_i \tag{13} $$

These corresponding point pairs ${}^{\text{base}}\mathbf{p}_i$ and ${}^{\text{phantom}}\mathbf{p}_i$ were then used to estimate ${}^{\text{base}}T_{\text{phantom}}$ using the method proposed by[34].

Following the initial positioning of the HIFU transducer, multiple sonications were performed at different spatial locations using 60%, 65%, and 70% of the maximum amplitude (0.33 MPa), with variable durations and a constant 90% duty cycle. The choosen acoustic power values were consistent with the range of clinically admissible values in case of tumor liver treatment[35]. In phantoms with a silicon top layer (PA+Eco and PA+PDMS), only a single exposure at 60% power was performed. This limitation was necessary due to the high acoustic impedance of the silicone, which poses a significant risk of excessive beam reflection that could irreversibly damage the HIFU transducer. Table 2 describes the sonication protocol adopted for each phantom.

Phantom	Shot #	Amplitude (%)	Duration (s)
PA, PA+PVA, PA+AGAR	1,2,3	60	45
	4,5,6	65	30
	7,8,9	70	10
PA+Eco	1	60	45
PA+PDMS	1	60	45

Table 2. Sonication protocol for different phantoms.

Performance metrics

Following sonications, the axial and transverse dimensions (D1 and D2) of the resulting lesions as well as the lesion depth were measured. Although our computational model is fully three-dimensional and capable of capturing lesion asymmetries, in this validation we assumed axial symmetry ($D_2 = D_3$), given the isotropic shape and material homogeneity of the phantoms. To ensure accurate and reproducible lesion assessment, a custom-designed cutting guide was fabricated. This device functioned as a cutting template, enabling precise sectioning of the PA layer along a predefined plane. The cutting plane was aligned to cut the lesions transversely at their midpoint, providing an optimal cross-sectional view for measurement and analysis. The guide was designed to match the phantom's dimensions and incorporated structural elements to secure the phantom during sectioning. This approach ensured consistent cross-sections, facilitating quantitative evaluation of lesion dimensions. To reduce any operator-dependent error, each measurement was performed five times, using a digital caliper, and the median value was considered. To validate the ablation position in both simulation and experiment, we first determined the lesion depth by measuring the distance from the PA top surface to the lesion's starting point and added D1/2. Next, we defined the ellipse defined by the median of the experimentally measured D1 and D2, centered at the measured lesion depth. Eventually, we quantified the spatial agreement between the simulated lesion and the experimental obtained one by computing the Dice Similarity Coefficient (DSC).

Translation on patient's anatomy

To assess the clinical feasibility of the proposed simulation framework for HIFU treatment, we translated our numerical model to a patient-specific case and implemented a dedicated planning tool, fully integrated within an interactive GUI. As a representative case study, we modeled HIFU treatment for liver tumor ablation. A contrast-enhanced abdominal CT scan (Medical Decathlon project dataset[36]) with an isotropic resolution of $0.699 \times 0.699 \times 0.699$ mm was imported into 3D Slicer[37]. The skin was manually segmented, while internal abdominal structures were automatically delineated using the TotalSegmentator tool[38]. These included subcutaneous fat, abdominal muscles, liver, hepatic vasculature, vertebrae, and ribs. All other internal organs were grouped under a single label, *'soft tissues'*, and treated as a unique medium. The segmented anatomical regions were converted to NIFTI format labelmaps and loaded into the GUI, where they were visualized in 3D along with the HIFU transducer and its corresponding ultrasound beam solid cone.

Based on the transducer's 3D pose within the scene, the system computed the percentage of fat and bone tissue intersected by the sonication cone. This information is critical for accurate treatment planning, given the distinct acoustic and thermal properties of these tissues. The user could interactively adjust the transducer's position and orientation within the interface, receiving real-time feedback on the beam trajectory and the intersected anatomical structures.

In order to meet the simulation grid requirements, a nearest-neighbor interpolation was performed on the labelmaps. To reduce the computational cost, only a selected region of interest containing the transducer was considered as computational domain in the simulation. This region was empirically modeled as a parallelepiped, with its width set to the transducer's diameter plus 1 cm, and its height fixed at 1.5 times the transducer's focal length. The simulation parameters for the segmented structures including the perfusion parameters of the liver vessels were defined based on the IT'IS database for thermal and electromagnetic parameters of biological tissues [39]. To assess the impact of anatomical structures on ultrasound propagation and the outcome of HIFU treatment, two simulations were conducted, varying the transducer position; the first one with partial bone obstruction

(2.90%) and the second one with no ribs intersection with solid cone representing the US beam propagation. In both cases, the same sonication parameters were used: a duty cycle of 90%, a sonication duration of 10 seconds, a transducer frequency of 1.2 MHz, and a power of 115 W for 50 seconds. These values are consistent with those reported in similar HIFU studies[40]. Given the anatomical complexity of patient-specific models, the geometric idealizations and homogeneity assumptions used in synthetic phantoms were no longer valid. In particular, axial symmetry of the lesion could not be assumed ($D_2 \neq D_3$); therefore, lesion dimensions were independently measured along all three axes (D_1, D_2, D_3) to account for anisotropic ablation effects.

Results

In vitro phantoms

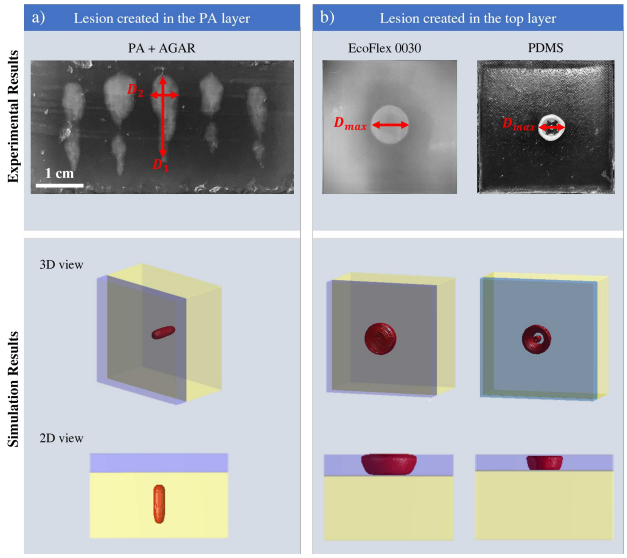

Figure 4. Overview of ablation results in both physical phantoms and the simulation environment. Panel a) shows a representative cross-sectional view from the PA+AGAR phantom, reflecting the same behavior of PA and PA+PVA, where all lesions formed within the PA layer. Panel b) presents two cases in which ablation was confined to the top layer, without extending into the underlying bottom layer.

To ensure the spatial accuracy of HIFU targeting during phantom experiments, robotic positioning was calibrated with high precision, yielding a root-mean-square error (RMSE) of 0.39 mm. This enabled accurate spatial alignment between the computational model and the physical setup, forming a consistent basis for simulation–experiment comparison. Phantoms composed of PA, PA+PVA and PA+AGAR exhibited similar behavior, with lesions consistently forming within the PA layer as planned (Figure 4.a, top panel). The phantom section enabled comparison of lesions produced under varying HIFU operating conditions, revealing highly irregular shapes. For these phantoms, both D1 and D2 dimensions were measurable. In contrast, phantoms with top layers consisting of EcoFlex 0030 and PDMS exhibited a different behavior, with lesions forming exclusively in the top layer. These materials attenuated the ultrasound beam, resulting in insufficient energy reaching the underlying PA layer to induce lesion formation (Figure 4.b, top panel). The reflection of the ultrasound waves produced circular surface lesions, for which diameters were measured. Simulation results, presented in Figure 4, bottom panel, confirmed the different behavior observed between the two phantom groups. Figure 5 shows the quantitative comparison between the experimental measuraments and the simulation output. D1 and D2 dimensions exhibited variations across phantom compositions and HIFU conditions, with experimental results showing general agreement with the corresponding simulation outputs.

Table 3 summarizes the D1 and D2 dimensions under both experimental and simulated conditions, along with the absolute error (in mm) between them.

Statistical analysis of these results was carried on performing the one-sample Wilcoxon signed-rank test. Across all experimental conditions, the experimental measurements did not exhibit any statistically significant deviation from the corresponding simulated value.

For the PA+Eco and PA+PDMS phantoms, the lesions were characterized by a circular shape with maximum lesion diameters (D_{max}) measured on the top layer of 17.50 mm and 12.10 mm, respectively. The corresponding simulations were able to predict circular ablations with diameters of 18.00 mm and 14.70 mm, thus resulting in an error of 0.50 mm and 2.60 mm respectively. Notably, the morphology of the simulated ablation zones closely resembled the experimental observations. In the

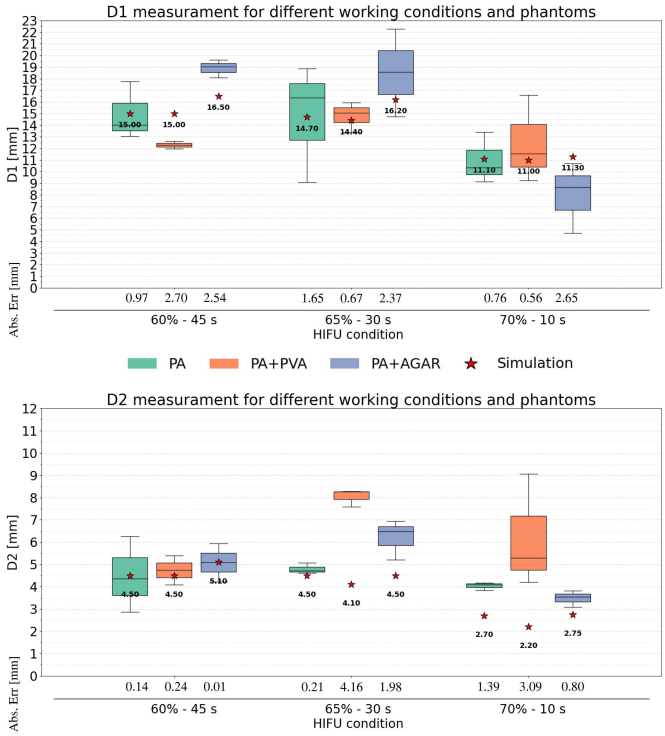

Figure 5. Experimental and simulated values for both the vertical (D1) and lateral (D2) dimensions of the ablation zones are reported, across three phantom types (PA, PA+PVA, PA+AGAR) and three HIFU exposure conditions (60%–45s, 65%–30s, 70%–10s). For each phantom-condition pair, the figure presents boxplots summarizing the full distribution of experimental measurements, alongside the corresponding simulation value (indicated by a red star). The barplot summarizes the absolute error between the median value and the simulation value.

case of EcoFlex0030, both simulation and experiment exhibited a disk-shaped lesion. For PDMS, both yielded two concentric, ring-shaped lesions. Figure 6 shows both the simulated and experimental lesion positions. For the PA phantom, the DSCs under the 60%–45 s, 65%–30 s and 70%–10 s HIFU conditions were 75%, 73% and 37%, respectively. In the PA+PVA phantom, these values were 89 %, 64% and 55%, while in the PA+AGAR phantom the DSCs reached 92%, 74% and 46%.

Patient specific anatomy

Figure 7 displays the simulated acoustic pressure field in the segmented model derived from the real anatomy. The pressure maps are shown on the sagittal plane for the two different simulations. In Figure 7 top panel, the ultrasound beam propagates through soft tissues, without intersecting bony structures. The focal region is clearly visible, with a maximum acoustic pressure of 3.11 MPa concentrated at the geometric focus. The beam remains tightly focused, producing a lesion with dimensions D1 = 4.20 mm, D2 = 14.70 mm, and D3 = 5.33 mm. The shift between the geometric focus and the centroid of the lesion Δl was 6.7 mm. In contrast, Figure 7 bottom panel illustrates the condition in which the beam intersects the rib cage (2.90%). Here, the peak focal pressure decreases to 1.87 MPa with a reduction of 40%. The lesion is notably smaller and more distorted, with dimensions D1 = 1.05 mm, D2 = 4.20 mm, and D3 = 1.78 mm. The presence of bone introduces partial reflection and scattering, resulting in visible beam distortion. The focal spot becomes less defined and the region of maximum intensity shifts towards the transducer with respect to the original geometric focus. In this case the shift Δl was 8.5 mm.

Simulation time

The computational times required to complete the acoustic simulations for the *in vitro* phantoms were: 11 minutes and 55 seconds for PA, 16 minutes and 12 seconds for PA+PVA, and 11 minutes and 16 seconds for PA+AGAR. The simulation times increased to 17 minutes and 15 seconds for PA+PDMS and 23 minutes and 7 seconds for PA+Eco. In the case of the real anatomy, the total computational time for each of the two simulated conditions was 32 minutes and 15 seconds.

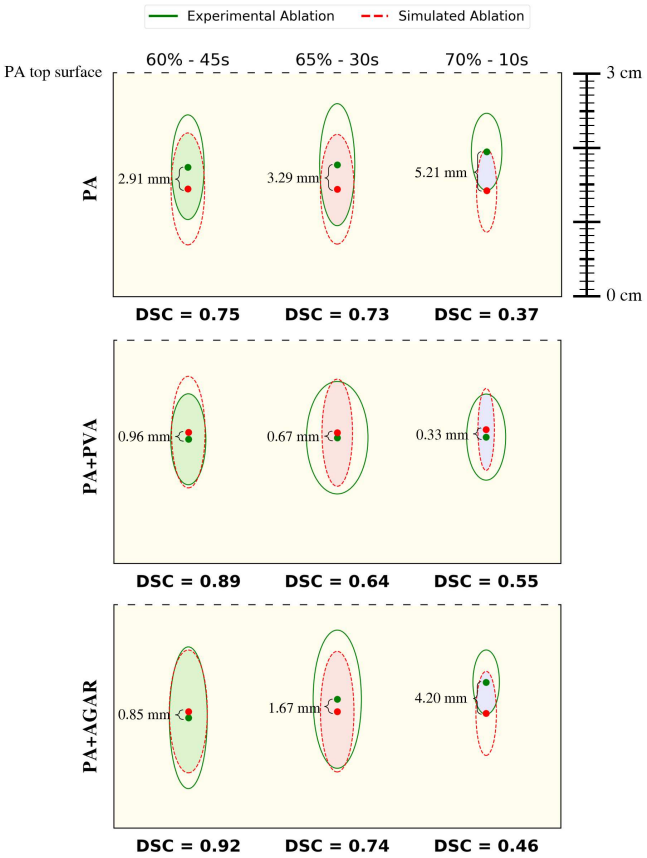

Figure 6. Experimental and simulated lesion positions for the three HIFU exposure conditions. To evaluate the accuracy in predicting the lesion position we measured the DSC between the ablation areas. The yellow rectangle represents the PA layer where the ablation formed, The colored patches (green,red and blue) represent the overlapping regions. The error between simulated (red dot) and experimental (green dot) lesions' center position is illustrated.

Discussion

This work presented a three-dimensional numerical simulation framework for HIFU treatment planning, developed using the k-Wave toolbox in MATLAB. The simulation enables the prediction of acoustic wave propagation in heterogeneous media and estimates the extent of thermal lesions resulting from focused ultrasound exposure. The approach was first validated on *in vitro* phantoms, and subsequently applied to simulate acoustic propagation in a real *in silico* patient's anatomy. The quantitative analysis demonstrated that the proposed simulation framework is capable of accurately predicting experimental ablation outcomes in the majority of cases. Specifically, for the D1 dimension, simulation results fell within the interquartile range of the experimental data in five out of nine phantom-condition combinations. For D2, this agreement was observed in three out of nine cases. Regarding the phantoms where lesions formed exclusively in the top layer (PA+PDMS and PA+Eco), the simulated maximum lesion diameters (D_{max}) correctly matched the corresponding experimental measurements. In our evaluation, the agreement between simulation and experiment was assessed by verifying whether the simulated value fell within the interquartile range of the experimental distribution, rather than relying solely on median discrepancies. This choice was motivated by the intrinsic variability of HIFU-induced lesions, which can differ significantly even under identical exposure conditions, due to the complex and nonlinear nature of acoustic and thermal propagation phenomena. This variability is particularly evident when repeating the same sonication multiple times, often leading to notable differences in lesion size and shape[5]. Such variability may also stem from inhomogeneities within the experimental phantoms themselves, arising from intrinsic inaccuracies in the fabrication process that can lead to local density variations. The results also reveal a greater discrepancy between simulated and experimentally measured lesion dimensions along the D2 axis compared to D1. In the experimental data, lesions appeared larger and asymmetrical along D2. While simulations predicted an ellipsoidal shape, the actual lesions exhibited a "tadpole-like" morphology, indicating the influence of a factor not accounted for in the computational model. This deviation is likely due to the boiling effect that occurs at high acoustic intensities when water-rich materials

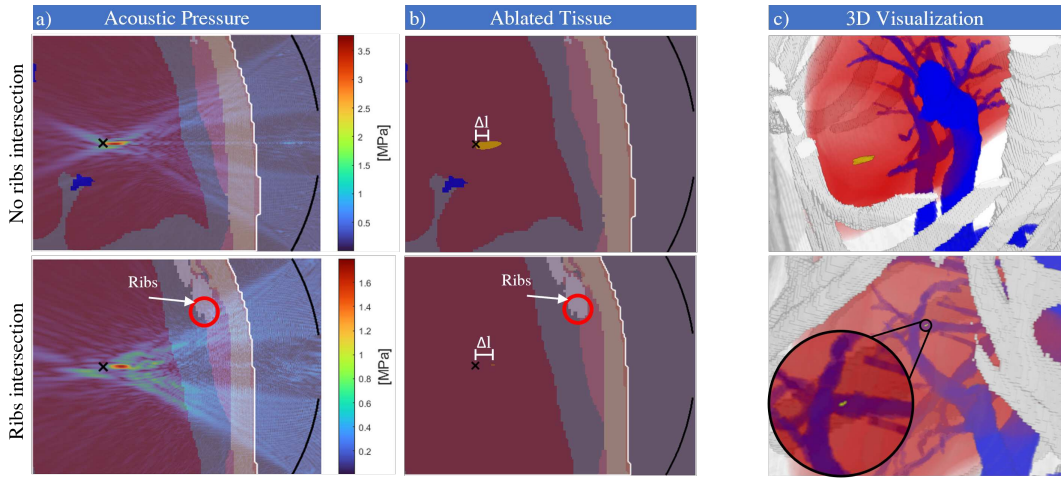

Figure 7. Simulation results on patient-specific anatomy without and with rib intersection, shown in the top and bottom panels, respectively. The black cross represents the geometric focus. a) Acoustic pressure propagation on the sagittal plane at the point of peak pressure. Hepatic vessels are shown in blue, liver in red, abdominal muscles in pink, fat in yellow, skin in white and the rest of *'soft tissues'* in grey b) Simulated ablated lesion (in orange) following HIFU treatment. Δl represents the shift in mm between the geometric focus and the centroid of the ablated volume c) 3D view of the GUI displaying the ablated volume within the liver. The fat layer is not rendered for visual clarity.

Phantom	Condition	D1			D2		
		Exp	Sim	Err	Exp	Sim	Err
PA	60%-45s	14.03	15.00	0.97	4.36	4.50	0.14
	65%-30s	16.35	14.70	1.65	4.71	4.50	0.21
	70%-10s	10.34	11.10	0.76	4.09	2.70	1.39
PA+PVA	60%-45s	12.30	15.00	2.70	4.74	4.50	0.24
	65%-30s	15.07	14.40	0.67	8.26	4.10	4.16
	70%-10s	11.56	11.00	0.56	5.30	2.20	3.09
PA+AGAR	60%-45s	19.04	16.50	2.54	5.09	5.10	0.01
	65%-30s	18.57	16.20	2.37	6.48	4.50	1.98
	70%-10s	8.65	11.30	2.65	3.55	2.75	0.80

Table 3. Median lesion dimensions (mm) for each phantom and condition: experimental (Exp), simulated (Sim), and absolute error (Err) for D1 and D2.

(such as our in vitro phantom, which contains a high water content) exceed 100°C, a temperature consistently reached in our simulations. During the experimental sonications, boiling behavior was actually observed, with bubble formation causing lesion expansion. The presence of vapor bubbles alters acoustic propagation by introducing scattering and reflection, ultimately resulting in radial lesion growth. This effect has been previously described in the literature[41]. Nonetheless, we reasonably deem that the discrepancy due to the boiling effect does not compromise the validation of the simulation. Indeed, the water content in biological tissues is significantly lower than in hydrogel phantoms, preventing boiling-induced effect in clinical scenarios. The lesions position results highlight a good correspondence between simulated and experimental scenarios, with DSCs reaching as high as 92% in the PA+AGAR. Notably, the 70%–10 s exposure condition consistently yielded the poorest overlap across all phantom types, whereas the 60%–45 s condition delivered the strongest agreement in two out of three cases (PA+PVA and PA+AGAR). Such a reduction in overlap can be attributed to the fact that, as acoustic power intensifies, the probability of cavitation phenomena[42] increases, a behavior not modeled in our current simulation framework.

Upon the *in vitro* validation, the simulations performed on patient-specific anatomy demonstrated the framework's ability to account for the heterogeneous properties of different tissues, including the perfusion effects of hepatic vessels, which can influence heat diffusion during treatment. Both simulations reveal that the actual focal point of the ultrasound beam does not coincide with the ideal geometric focus in either scenario. In both cases, the focus is shifted towards the transducer, although the extent and nature of this change (Δl) vary depending on the anatomical configuration, with a higher value in the case of rib intersection. This displacement is primarily due to the interaction between the ultrasound beam and the interposed tissues. The simulation accounts for the presence of different anatomical structures, each with distinct acoustic properties and surface

irregularities, that influence wave propagation through reflection, refraction, and scattering. In the case where the beam travels through only soft tissues, the focus remains relatively sharp and well-defined. However, when the beam intersects the rib cage, partial reflection and scattering introduced by the bone significantly distort the beam path. This results in a substantial drop in peak focal pressure and a notable reduction in thermal lesion dimensions.

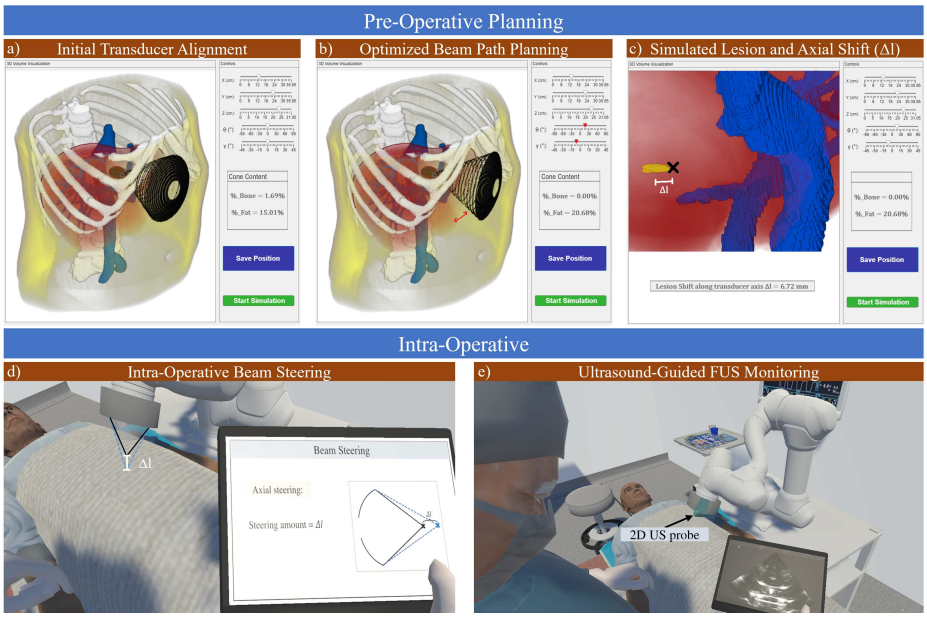

Figure 8. Proposed pipeline integrating the developed GUI as a planning support tool in HIFU therapy. a) Initial coarse positioning of the transducer with the geometric focus on the clinical target (brown tumor), including visualization of intersected tissues. b) If bone is intersected, the transducer pose is optimized to avoid it while maintaining target alignment. c) Simulation computes the actual ablated volume and its axial shift (Δl) from the geometric focus (black cross). d) Intraoperatively, Δl is compensated via electronic beam steering without moving the transducer. e) Lesion formation is monitored in real time using a coaxial ultrasound probe to ensure target conformity.

The developed GUI provides an intuitive and interactive 3D visualization environment that facilitates treatment planning. It allows for the rendering of patient-specific anatomy, transducer positioning, and the geometric representation of the ideal ultrasound beam path in fully 3D fashion. In the envisioned clinical application (Figure 8), the operator can first align the transducer such that its geometric focus coincides with the clinical target zone. More importantly, the user can assess whether the acoustic beam intersects undesired structures, particularly bones and optimize beam targeting through dynamic adjustment of the transducer's position and orientation. Once a satisfactory configuration is established the simulation can be launched. The predicted thermal lesion is then rendered within the anatomical model, providing immediate visual feedback on its location, morphology, and axial displacement relative to the intended target. This comprehensive 3D visualization facilitates preoperative decision-making by enabling clinicians to anticipate treatment deviations and apply corrective strategies, such as electronic beam steering, to compensate for axial focal shifts. The entire pipeline, from image acquisition to final simulation, is computationally efficient and compatible with clinical workflows. The full simulation requires approximately 32 minutes, with ancillary steps such as skin segmentation, automated segmentation of organs, and region of interest extraction, executed within a few additional minutes.

While the present study yields encouraging results, the collected data is still limited and should be expanded to enable a more robust validation. In addition, the envisioned clinical applicability should be validated on *ex-vivo* tissues. Eventually, porting the numerical simulation to a C++ implementation could reduce computational time, thereby enhancing its suitability for integration into routine clinical workflows.

Conclusion

Although intraoperative ultrasound imaging is commonly used to monitor HIFU ablation in US-guided-HIFU, it only provides visual feedback after energy delivery has occurred. As such, it does not prevent mistargeting before energy delivery. The proposed framework paves the way to precise targeting and reduction of unintended tissue damage during treatment. By integrating *in vitro* validated simulation, anatomical modeling, and interactive 3D visualization into a unified tool, we present a

reproducible and clinically supportive planning paradigm for HIFU therapy. The proposed pipeline has the potential to enhance treatment accuracy, improve clinical safety, and support the broader adoption of HIFU as a non-invasive therapeutic modality in routine clinical practice.

Data availability

All data generated or analysed during this study are included in this published article [and its supplementary information files].

References

1. Ter Haar, G. Hifu tissue ablation: concept and devices. *Ther. ultrasound* 3–20 (2016).
2. Elhelf, I. S. *et al.* High intensity focused ultrasound: The fundamentals, clinical applications and research trends. *Diagn. interventional imaging* **99**, 349–359 (2018).
3. O'Reilly, M. A. Exploiting the mechanical effects of ultrasound for noninvasive therapy. *Science* **385**, eadp7206, DOI: 10.1126/science.adp7206 (2024). https://www.science.org/doi/pdf/10.1126/science.adp7206.
4. Shehata, I. A. Treatment with high intensity focused ultrasound: secrets revealed. *Eur. journal radiology* **81**, 534–541 (2012).
5. Simoni, V., Cafarelli, A., Tognarelli, S. & Menciassi, A. Ex vivo assessment of multiple parameters in high intensity focused ultrasound. In *2018 40th Annual International Conference of the IEEE Engineering in Medicine and Biology Society (EMBC)*, 5705–5708 (IEEE, 2018).
6. Izadifar, Z., Izadifar, Z., Chapman, D. & Babyn, P. An introduction to high intensity focused ultrasound: systematic review on principles, devices, and clinical applications. *J. clinical medicine* **9**, 460 (2020).
7. Zhou, Y.-F. High intensity focused ultrasound in clinical tumor ablation. *World journal clinical oncology* **2**, 8 (2011).
8. Gunderman, A., Montayre, R., Ranjan, A. & Chen, Y. Review of robot-assisted hifu therapy. *Sensors* **23**, 3707 (2023).
9. Mariani, A., Morchi, L., Diodato, A., Tognarelli, S. & Menciassi, A. High-intensity focused ultrasound surgery based on kuka robot: A computer-assisted platform for noninvasive surgical treatments on static and moving organs. *IEEE Robotics & Autom. Mag.* **30**, 79–93 (2022).
10. Hinkelman, L. M., Mast, T. D., Metlay, L. A. & Waag, R. C. The effect of abdominal wall morphology on ultrasonic pulse distortion. part i. measurements. *The J. Acoust. Soc. Am.* **104**, 3635–3649 (1998).
11. Mast, T. D., Hinkelman, L. M., Orr, M. J. & Waag, R. C. The effect of abdominal wall morphology on ultrasonic pulse distortion. part ii. simulations. *The J. Acoust. Soc. Am.* **104**, 3651–3664 (1998).
12. Amin, V., Roberts, R., Long, T., Thompson, R. B. & Ryken, T. A study of effects of tissue inhomogeneity on hifu beam. In *AIP Conference Proceedings*, vol. 829, 201–205 (American Institute of Physics, 2006).
13. Thomas, G. P. L. *et al.* Phase-aberration correction for hifu therapy using a multielement array and backscattering of nonlinear pulses. *IEEE Transactions on Ultrason. Ferroelectr. Freq. Control.* **68**, 1040–1050, DOI: 10.1109/TUFFC.2020.3030890 (2021).
14. Aubry, J.-F., Pernot, M., Marquet, F., Tanter, M. & Fink, M. Transcostal high-intensity-focused ultrasound: ex vivo adaptive focusing feasibility study. *Phys. Medicine & Biol.* **53**, 2937 (2008).
15. Dasgupta, S., Banerjee, R. K., Hariharan, P. & Myers, M. R. Beam localization in hifu temperature measurements using thermocouples, with application to cooling by large blood vessels. *Ultrasonics* **51**, 171–180 (2011).
16. Diodato, A. *et al.* Motion compensation with skin contact control for high intensity focused ultrasound surgery in moving organs. *Phys. Medicine & Biol.* **63**, 035017 (2018).
17. Wilcox, S., Huang, Z., Shah, J., Yang, X. & Chen, Y. Respiration-induced organ motion compensation: A review. *Annals Biomed. Eng.* **53**, 271–283 (2025).
18. Marquet, F. *et al.* In-vivo non-invasive motion tracking and correction in high intensity focused ultrasound therapy. In *2006 International Conference of the IEEE Engineering in Medicine and Biology Society*, 688–691 (IEEE, 2006).
19. Aslani, P. *et al.* Thermal therapy with a fully electronically steerable hifu phased array using ultrasound guidance and local harmonic motion monitoring. *IEEE Transactions on Biomed. Eng.* **67**, 1854–1862 (2019).
20. Daniel, M., Attali, D., Tiennot, T., Tanter, M. & Aubry, J. Multifrequency transcranial ultrasound holography with acoustic lenses. *Phys. Rev. Appl.* **21**, 014011, DOI: 10.1103/PhysRevApplied.21.014011 (2024).

21. Montienthong, P. & Rattanadecho, P. Focused ultrasound ablation for the treatment of patients with localized deformed breast cancer: Computer simulation. *J. Heat Transf.* **141**, 101101 (2019).

22. Safisamghabadi, M. *Numerical and Experimental Investigation of Scattering of Focused Ultrasonic Waves at Solid-fluid Interfaces*. Ph.D. thesis, California State University, Northridge (2018).

23. Multiphysics, C. Introduction to comsol multiphysics®. *COMSOL Multiphysics, Burlington, MA, accessed Feb* **9**, 2018 (1998).

24. Treeby, B. E. & Cox, B. T. k-wave: Matlab toolbox for the simulation and reconstruction of photoacoustic wave fields. *J. biomedical optics* **15**, 021314–021314 (2010).

25. Martin, E., Jaros, J. & Treeby, B. E. Experimental validation of k-wave: Nonlinear wave propagation in layered, absorbing fluid media. *IEEE transactions on ultrasonics, ferroelectrics, frequency control* **67**, 81–91 (2019).

26. Rosnitskiy, P. B., Khokhlova, T. D., Schade, G. R., Sapozhnikov, O. A. & Khokhlova, V. A. Treatment planning and aberration correction algorithm for hifu ablation of renal tumors. *IEEE Transactions on Ultrason. Ferroelectr. Freq. Control.* (2024).

27. Treeby, B. E. & Cox, B. T. *k-Wave User Manual*. Department of Medical Physics and Biomedical Engineering, University College London, London, United Kingdom (2010). Version 1.1.

28. Westervelt, P. J. Parametric acoustic array. *The J. acoustical society Am.* **35**, 535–537 (1963).

29. Lafon, C., Kaczkowski, P. J., Vaezy, S., Noble, M. & Sapozhnikov, O. A. Development and characterization of an innovative synthetic tissue-mimicking material for high intensity focused ultrasound (hifu) exposures. In *2001 IEEE Ultrasonics Symposium. Proceedings. An International Symposium (Cat. No. 01CH37263)*, vol. 2, 1295–1298 (IEEE, 2001).

30. Earle, M., De Portu, G. & DeVos, E. Agar ultrasound phantoms for low-cost training without refrigeration. *Afr. J. Emerg. Medicine* **6**, 18–23 (2016).

31. Sharma, A. *et al.* Characterizing viscoelastic polyvinyl alcohol phantoms for ultrasound elastography. *Ultrasound Medicine & Biol.* **49**, 497–511 (2023).

32. Smooth-On, Inc. *Ecoflex™ 00-30 Technical Data Sheet* (2024).

33. Goldfain, A. M., Lemaillet, P., Allen, D. W., Briggman, K. A. & Hwang, J. Polydimethylsiloxane tissue-mimicking phantoms with tunable optical properties. *J. biomedical optics* **27**, 074706–074706 (2022).

34. Horn, B. K., Hilden, H. M. & Negahdaripour, S. Closed-form solution of absolute orientation using orthonormal matrices. *J. Opt. Soc. Am. A* **5**, 1127–1135 (1988).

35. Kennedy, J. *et al.* High-intensity focused ultrasound for the treatment of liver tumours. *Ultrasonics* **42**, 931–935 (2004).

36. Antonelli, M. *et al.* The medical segmentation decathlon. *Nat. communications* **13**, 4128 (2022).

37. 3D Slicer Community. 3d slicer: A multi-platform open source software for medical image computing (2024). Accessed: 16 February 2025.

38. Wasserthal, J. N. *et al.* TotalSegmentator: robust segmentation of 104 anatomical structures in ct images. *arXiv preprint arXiv:2208.05868* (2022). Accessed: 19 February 2025.

39. IT'IS Foundation. Tissue properties database version 4.2 (2022).

40. Kim, Y.-s. *et al.* Volumetric mr-hifu ablation of uterine fibroids: role of treatment cell size in the improvement of energy efficiency. *Eur. journal radiology* **81**, 3652–3659 (2012).

41. Khokhlova, V. A. *et al.* Effects of nonlinear propagation, cavitation, and boiling in lesion formation by high intensity focused ultrasound in a gel phantom. *The J. Acoust. Soc. Am.* **119**, 1834–1848 (2006).

42. Wu, J. & Nyborg, W. L. Ultrasound, cavitation bubbles and their interaction with cells. *Adv. drug delivery reviews* **60**, 1103–1116 (2008).

Acknowledgements

We gratefully acknowledge PhD Tatiana Mencarini for her valuable expertise and support in the fabrication of the phantoms used for validation.

Funding

This work was supported by the Italian Ministry of University and Research (MUR) under the PRIN 2022 program (Progetti di Rilevante Interesse Nazionale), project code 2022342MEF, titled FUtuRo - Focused Ultrasound Surgery enabled by Robotics and Simulation.

Author contributions statement

F. Morelli and A. Albanesi conceived the study, coordinated the research activities, designed the phantoms, and carried out the experiments. A. Ivanaj contributed to the computational modeling of the acoustic and thermal simulations as well as to the development of the graphical user interface. J. Fu, S. Buratti, F. Parrotta, and S. Tognarelli assisted with the experimental design, the setup of the robotic HIFU platform, and the analysis of the results. A. Menciassi, E. De Momi, and A. Redaelli supervised the overall project. All authors discussed the results, contributed to the manuscript preparation, and approved its final version.

Declarations

Competing interests

The authors declare no competing interests

Supplementary Files

This is a list of supplementary files associated with this preprint. Click to download.

- rawexperimentdata.xlsx